

Article

Ion and Water Transports in Double Gyroid Nanochannels Formed by Block Copolymer Anion Exchange Membranes

Karim Aissou ^{1,*}, Maximilien Coronas ¹, Jason Richard ¹, Erwan Ponsin ¹, Sambhav Vishwakarma ¹, Eddy Petit ¹, Bertrand Rebiere ², Camille Bakkali-Hassani ³, Stéphanie Roualdes ¹ and Damien Quemener ¹

¹ Institut Européen des Membranes, IEM, UMR 5635, Univ Montpellier, ENSCM, CNRS, Montpellier, France; maximilien.coronas@umontpellier.fr (M.C.); jason.richard@umontpellier.fr (J.R.); erwan.ponsin@umontpellier.fr (E.P.); sambhav.vishwakarma@umontpellier.fr (S.V.); eddy.petit@umontpellier.fr (E.P.); stephanie.roualdes@umontpellier.fr (S.R.); damien.quemener@umontpellier.fr (D.Q.)

² PAC Chimie Balard, Univ Montpellier, CNRS, ENSCM, Montpellier, France; bertrand.rebiere@umontpellier.fr

³ Institut Charles Gerhardt Montpellier, ICGM, UMR 5253, Univ Montpellier, ENSCM, CNRS, Montpellier, France; camille.bakkali-hassani@umontpellier.fr

* Correspondence: karim.aissou@umontpellier.fr

Abstract: Mechanically improved polymeric membranes with high ionic conductivity (IC) and good permeability are highly desired for next-generation anion exchange membranes (AEMs) in order to reduce Ohmic losses and enhance water management in alkaline membrane fuel cells. To move towards the fabrication of such high-performance membranes, the creation of hydrophilic ion-conducting double gyroid (DG) nanochannels within block copolymer (BCP) AEMs is a promising approach. However, this attractive solution remains difficult to implement due to the complexity of constructing a well-developed ion-conducting DG morphology across the entire membrane thickness. To deal with this issue, water permeable polystyrene-*block*-poly(2-vinylpyridine)-*block*-poly(ethylene oxide) membranes with ion-conducting DG nanochannels were produced by combining a solvent vapor annealing (SVA) treatment with a methylation process. Here, the SVA treatment enabled the manufacture of DG-forming BCP AEMs while the methylation process allowed for the conversion of pyridine sites to *N*-methylpyridinium (NMP^+) cations via a Menshutkin reaction. Following this SVA-methylation method, the IC value of water-permeable ($\sim 384 \text{ L h}^{-1} \text{ m}^{-2} \text{ bar}^{-1}$) DG-structured BCP AEMs in their OH^- counter anion form was measured to be of $\sim 2.8 \text{ mS.cm}^{-1}$ at 20°C while a lower IC value was probed, under the same experimental conditions, from as-cast NMP^+ -containing analogs with a non-permeable disordered phase ($\sim 1.2 \text{ mS.cm}^{-1}$).

Keywords: solvent vapor annealing; block copolymer electrolyte; self-assembly; double-gyroid; ionic conductivity



Academic Editor: George Zheng Chen

Received: 27 February 2025

Revised: 19 March 2025

Accepted: 21 March 2025

Published: 26 March 2025

Citation: Aissou, K.; Coronas, M.; Richard, J.; Ponsin, E.; Vishwakarma, S.; Petit, E.; Rebiere, B.; Bakkali-Hassani, C.; Roualdes, S.; Quemener, D. Ion and Water Transports in Double Gyroid

Nanochannels Formed by Block Copolymer Anion Exchange

Membranes. *Batteries* **2025**, *11*, 126.

<https://doi.org/10.3390/batteries11040126>

batteries11040126

Copyright: © 2025 by the authors. Licensee MDPI, Basel, Switzerland. This article is an open access article distributed under the terms and conditions of the Creative Commons Attribution (CC BY) license (<https://creativecommons.org/licenses/by/4.0/>).

1. Introduction

Nowadays, the majority of world energy production still comes from the combustion of fossil fuels (e.g., coal, oil, and gas), which contributes to air pollution and produces carbon dioxide, considered as the largest driver of global climate. To address these environmental impacts as well as the depletion of conventional fossil fuels, many efforts have been deployed to look for new power generation methods in the past decades.

Among the various alternative energies employed to accelerate the transition towards a carbon-free world, polymer electrolyte membrane-based technologies such as fuel cells are envisioned as promising solutions with high efficiency to replace conventional power

generation technologies relying on fossil fuels [1,2]. In principle, the polymer electrolyte membrane fuel cells are divided into two types [3–5]: the anion exchange membrane fuel cells (AEMFCs) and the proton exchange membrane fuel cells (PEMFCs), including the gold standard Nafion® 211 membrane having a conductivity value of $\sim 70 \text{ mS.cm}^{-1}$ at 25°C [6].

The AEMFCs have the advantage over PEMFCs in that they allow for the use of lower cost non-noble metal catalysts [7] and avoid the use of fluorinated polymers [8], thereby offering potential cost reductions. Despite these significant advantages, to make progress in the race to achieve better AEMFC performances, their anion exchange membranes (AEMs), consisting of positive charges tethered on the polymer backbone and mobile hydroxide ions, still have to demonstrate advances regarding: (i) the trade-off between high ionic conductivity (IC) and mechanical robustness, (ii) water management, and (iii) chemical stability in highly basic conditions [9–11].

To alleviate the trade-off mentioned above, the concept of using hydrophobic-hydrophilic block copolymer (BCP) AEMs, endowed with ion-conducting nanochannels integrated inside an insulating and robust polymer matrix, is revealed to be a successful strategy [12–14]. Indeed, although a lack of morphology control is generally observed, it has been shown that nanophase-separated BCP AEMs with continuous but disordered water-swollen ion-conducting pathways have higher ICs compared to their random copolymer counterparts [15–19].

Apart from its crucial role in achieving a fast ion transport, the creation of hydrophilic ion conductive nanochannels, with physical continuity through the entire membrane thickness, is also highly desired to overcome water management issues. Indeed, a high water back diffusion (i.e., anode water removal towards the cathode), favored by high water transport properties, is needed to avoid cathode dry-out and anode flooding occurring invariably in AEMFCs [10,20–22]. Furthermore, the cathode dry-out decreases locally the number of water molecules solvating hydroxide anions, which promotes the instability of cationic groups through hydroxide attack, thereby leading to degradation and loss of performance [11,23].

To maximize both the IC and water transport within AEMs, a nanostructure with perfectly aligned and uninterrupted nanochannels from one electrode to another is preferred since vertically aligned hydrophilic ion-conducting pathways have a tortuosity equal to unity [24]. However, controlling the nanochannel orientation within several micrometer-thick membranes remains challenging. To circumvent this issue, the Nealey group [25,26] have recently studied the in-plane IC of vertically aligned lamellae formed within sub-50 nm thick polystyrene-*block*-poly(2-vinyl pyridine) (PS-*b*-P2VP) layers in which cationic *N*-methylpyridinium (NMP^+) centers with iodides as counter-ions were introduced into P2VP nanodomains via a Menshutkin reaction. They found that the in-plane IC of a defect-free morphology with fully connected and aligned P2VP-based nanodomains ($\sim 2 \text{ mS.cm}^{-1}$ at 25°C and 95% RH) was more than an order of magnitude higher than that measured from a morphology exhibiting defects and grain boundaries. To push further this concept, a methodology capable of fabricating several micrometers-thick BCP AEMs with long range-ordered continuous and alignment-free ion-conducting nanodomains is highly desired. This can be achieved through the creation a double gyroid (DG) morphology within the BCP AEM since the DG phase, having a moderate tortuosity of ~ 1.25 [27], can transport ions in all three directions, thereby facilitating the evaluation of anion conduction perpendicular to the membrane (i.e., in the more relevant through-plane direction). Indeed, the DG structure is a triply periodic minimal surface (TPMS) with zero mean curvature that extends periodically in all three spatial directions, reducing energy barriers for ion diffusion across grain boundaries and enhancing transport efficiency [28]. Unlike continuous but

disordered ion-conducting pathways, periodic 3D-interconnected nanochannels provide a structural advantage for fabricating optimized membranes with precisely controllable critical parameters (e.g., pathway connectivity and tortuosity) since TPMS-based structures can be precisely defined using mathematical functions [29]. For instance, hydroxide ion transport within 1 nm-scale DG nanochannels formed by liquid-crystalline AEMs has been recently reported [30]. However, while nanostructured polymerized ionic liquid (PIL) BCPs have also been studied [31], a clear DG structure has yet to be demonstrated within PIL BCP AEMs. This phenomenon may be due to the disordering effect of electrostatic interactions that stabilize the homogenous phase, as predicted by self-consistent field theory (SCFT) [32] and random phase approximation (RPA) [33], particularly when the degree of charge within the ionomer block is high.

To avoid this phase behavior, we propose to use an amphiphilic ABC-type BCP (namely, PS-*b*-P2VP-*b*-poly(ethylene oxide) (PS-*b*-P2VP-*b*-PEO)) to generate DG-forming AEMs having excellent ion and water transport properties. As the formation of well-developed nanostructures remains challenging to achieve from self-assembled charge-containing BCP chains, the DG phase was first created within neutral PS-*b*-P2VP-*b*-PEO films by a using solvent vapor annealing (SVA) treatment. A methyl iodide (CH_3I) vapor was then used to produce water-permeable ($\sim 384 \text{ L h}^{-1} \text{ m}^{-2} \text{ bar}^{-1}$) hydrophilic DG nanochannels in which pyridine sites were partly converted (~52%) to *N*-methylpyridinium cations with iodides as counter-ions. Following an ion-exchange strategy, a through-plane conductivity value as high as $\sim 2.8 \text{ mS.cm}^{-1}$ was measured at 20°C from a $25 \mu\text{m}$ thick hydrated AEM entirely composed of a DG structure in its OH^- counter anion form. This OH^- transport value was found to be more than 2 times higher than that measured from an as-cast hydrated analog, consisting of a thick substructure with a non-water permeable disordered (DIS) phase and a thin skin layer exhibiting short-range ordered nanodomains ($\sim 1.2 \text{ mS.cm}^{-1}$ at 20°C).

2. Results

As achieving a highly ordered TPMS nanostructure from a microphase-separated charged-neutral BCP system is generally more challenging, our strategy was to generate a DG morphology through the self-assembly of neutral PS-*b*-P2VP-*b*-PEO chains ($\text{S:2VP:EO} \approx 65:22:13$, $69.5 \text{ kg}\cdot\text{mol}^{-1}$) before introducing cationic sites into the hydrophilic nanochannels via a methylation reaction. Figure 1 illustrates the process route used to manufacture DG-forming AEMs, with effective ion and water transportation capacities. For that purpose, a $25 \mu\text{m}$ -thick PS-*b*-P2VP-*b*-PEO film was first cast onto a ($3 \times 3 \text{ cm}$) silicon substrate covered by a $14 \mu\text{m}$ -thick poly(3,4-ethylenedioxythiophene):polystyrene sulfonate (PEDOT:PSS) sacrificial layer. The nominally as-cast morphology was then transformed into a well-developed DG structure by using a SVA treatment (15 h, dichloromethane (DCM)) as shown on the associated atomic force microscopy (AFM) topographic images. A *N*-methylpyridinium-based membrane in its iodide counter anion form is finally produced by exposing the DG-structured PS-*b*-P2VP-*b*-PEO film to a methyl iodide vapor for 4 h inside a sealed jar containing typically a $500 \mu\text{L}$ solution of CH_3I , as shown on the schematic reaction diagram.

Interestingly, the corresponding AFM topographic image shows that the DG nanostructure is not destroyed after the methylation process using a $500 \mu\text{L}$ CH_3I solution, although the fineness of the double-wave pattern formed on the DG (211) plane is slightly altered. It is noteworthy that the double-wave pattern is considerably affected (i.e., not clearly observable by AFM) when the DG-structured AEM is exposed to a $700 \mu\text{L}$ CH_3I solution for 4 h, a condition beyond the scope of this study, which focuses on the formation of a well-developed TPMS nanostructure.

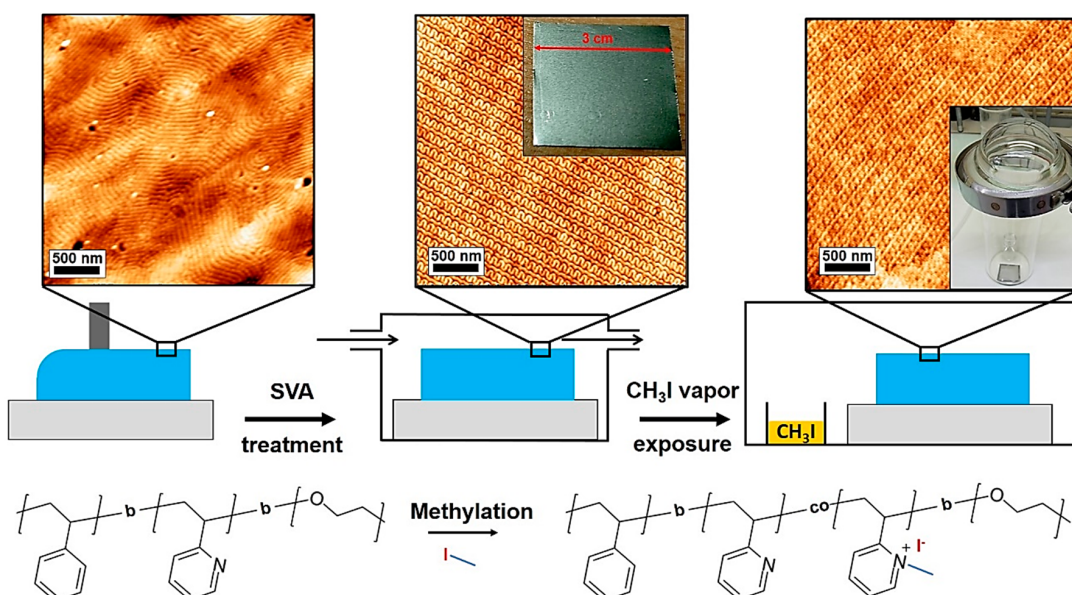


Figure 1. Schematic illustration of the process route used to manufacture a DG-forming BCP AEM having effective ion and water transportation capacities. To this end, the short-range ordered morphology generated on the film's top surface during the casting process (step 1) is first transformed into a highly ordered DG structure after the SVA treatment (15 h, DCM, step 2). A subsequent exposure to a CH₃I vapor for 4 h enables the formation of NMP⁺ centers with iodides as counterions on pyridine sites via a Menshutkin reaction (step 3) (see also the schematic reaction diagram). AFM topographic images were taken after each step of the manufacturing process to capture the morphology evolution of the film's top surface. The pictures show a 25 μm thick PS-*b*-P2VP-*b*-PEO film at different stages of the fabrication process: (step 2) cast onto a (3 \times 3 cm) substrate covered by a PEDOT:PSS layer, (step 3) placed into a sealed jar containing a 500 μL CH₃I solution, and (right) detached from the substrate and cut into a freestanding 2.5 cm diameter disc.

The cross-section scanning electron microscopy (SEM) image presented in Figure S1a shows that a DIS phase (i.e., a morphology without nanochannel formation) is quenched within the substructure of a 25 μm -thick PS-*b*-P2VP-*b*-PEO film during the casting process. This behavior indicates that the short-range ordered morphology formed on the film's free surface is unable to grow at the expense of the substructure during the deposition process due to a rapid and uncontrollable evaporation rate of solvent (see Figure S1b). In contrast, a well-developed DG structure with large grains is produced throughout the entire film thickness by exposing the PS-*b*-P2VP-*b*-PEO chains to a DCM vapor for 15 h (see Figure 2A–C). As the AFM data indicate that the 14 μm -thick PEDOT:PSS sacrificial layer covering the Si substrate has a low average roughness (R_a) of ~13.6 nm after exposure to SVA followed by washing with a DOX/THF solution (see Figure S2a), the rough bottom surface observed in Figure 2D is expected to form during SVA treatment, possibly due to a dewetting phenomenon. For instance, a maximum peak-to-valley roughness above 0.5 μm was measured from the (10 \times 10 μm) AFM topographic image presented in Figure S2b.

To study the conversion of pyridine sites to cationic NMP⁺ centers within the DG nanochannels via a methylation reaction, the solvent-annealed (15 h, DCM) PS-*b*-P2VP-*b*-PEO films were placed in a sealed jar containing a 500 μL CH₃I solution. In order to allow a full evaporation of the CH₃I solution, and thus an effective Menshutkin reaction, the methylation process was carried out for 4 h inside the sealed jar maintained at 25 °C. Figure 3A shows the Fourier-transform infrared (FTIR) traces for the DG-forming BCP films before and after reaction with 500 μL of CH₃I reagent in the range of 1500–2000 cm^{-1} (i.e., where both the pyridine (C–N) and *N*-methylpyridinium (C–N⁺) stretching bands are visible). After the methylation reaction in the sealed jar, it is found that the C–N stretching

vibration mode of the free P2VP band, observed in the range of $1570\text{--}1590\text{ cm}^{-1}$, decreases while a new C–N⁺ band is formed at 1630 cm^{-1} . A similar behavior is observed from an as-cast terpolymer film placed in a sealed jar containing a $500\text{ }\mu\text{L}$ CH₃I solution. These results are also confirmed by a strong increase of the broad O–H signal band (stretching at 3500 cm^{-1}) displayed on the FTIR spectra presented in Figure 3B. Indeed, as NMP⁺ cations with iodides as counter-ions are more hydrophilic than pyridine sites, the binding of atmospheric water to the PS-*b*-P2VP-*b*-PEO film is facilitated by the quaternization of pyridine sites. To determine the fraction of pyridine sites converted to NMP⁺ cations with iodides as counter-ions after the methylation reaction using $500\text{ }\mu\text{L}$ of reagent, X-ray photoelectron spectroscopy (XPS) was used (see Figure 3C). The N1s XPS spectrum, recorded before exposing the DG-structured PS-*b*-P2VP-*b*-PEO film to a CH₃I vapor, exhibits a single peak with a binding energy of 398.9 eV . In contrast, a shift of a peak fraction of the N1s core level by $\sim 3\text{ eV}$ (i.e., to 401.9 eV) confirms the formation of NMP⁺ cations after a 4 h reaction with a CH₃I vapor. Integration of the two peaks reveals that the fraction of cationic NMP⁺ centers within the DG nanochannels is ~ 0.52 ($\text{Area}_{\text{C}-\text{N}^+}/\text{Area}_{\text{C}-\text{N}}$). A comparable degree of conversion of pyridine sites into NMP⁺ centers ($\text{Area}_{\text{C}-\text{N}^+}/\text{Area}_{\text{C}-\text{N}} \approx 0.51$) was also observed for the as-cast terpolymer layer after a 4 h exposure to a CH₃I vapor. For both the as-cast and DG-structured films, the presence of iodide as counter-ion was confirmed by the I3d XPS spectra shown in Figure S3 from which the I3d_{3/2} (617.8 eV) and I3d_{5/2} (629.4 eV) peaks are clearly visible. Note that although the double-wave pattern of the (211) plane of the DG structure is considerably affected after exposing the BCP AEM to a $700\text{ }\mu\text{L}$ CH₃I solution for 4 h, XPS data reveal that the degree of conversion of pyridine sites into NMP⁺ centers does not significantly increase under these conditions ($\text{Area}_{\text{C}-\text{N}^+}/\text{Area}_{\text{C}-\text{N}} \approx 0.55$).

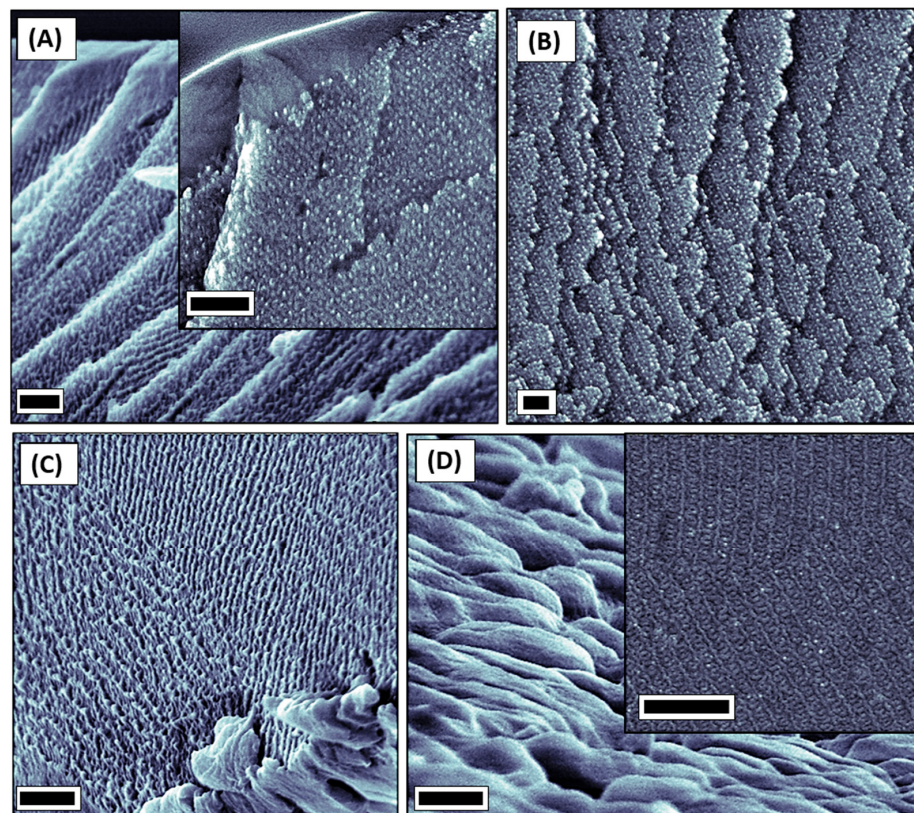


Figure 2. Cross-sectional SEM views of a solvent-annealed (15 h, DCM) PS-*b*-P2VP-*b*-PEO layer showing the presence of a well-defined DG structure in the vicinity of the (A) top, (B) middle, and

(C) bottom film regions, thereby confirming this 3D-interconnected morphology has growth at the expense of the DIS phase during the SVA treatment. (D) Top view SEM image showing that the bottom surface of the PS-*b*-P2VP-*b*-PEO film is rough in comparison with the top surface shown in the inset. Scale bars: 500 nm.

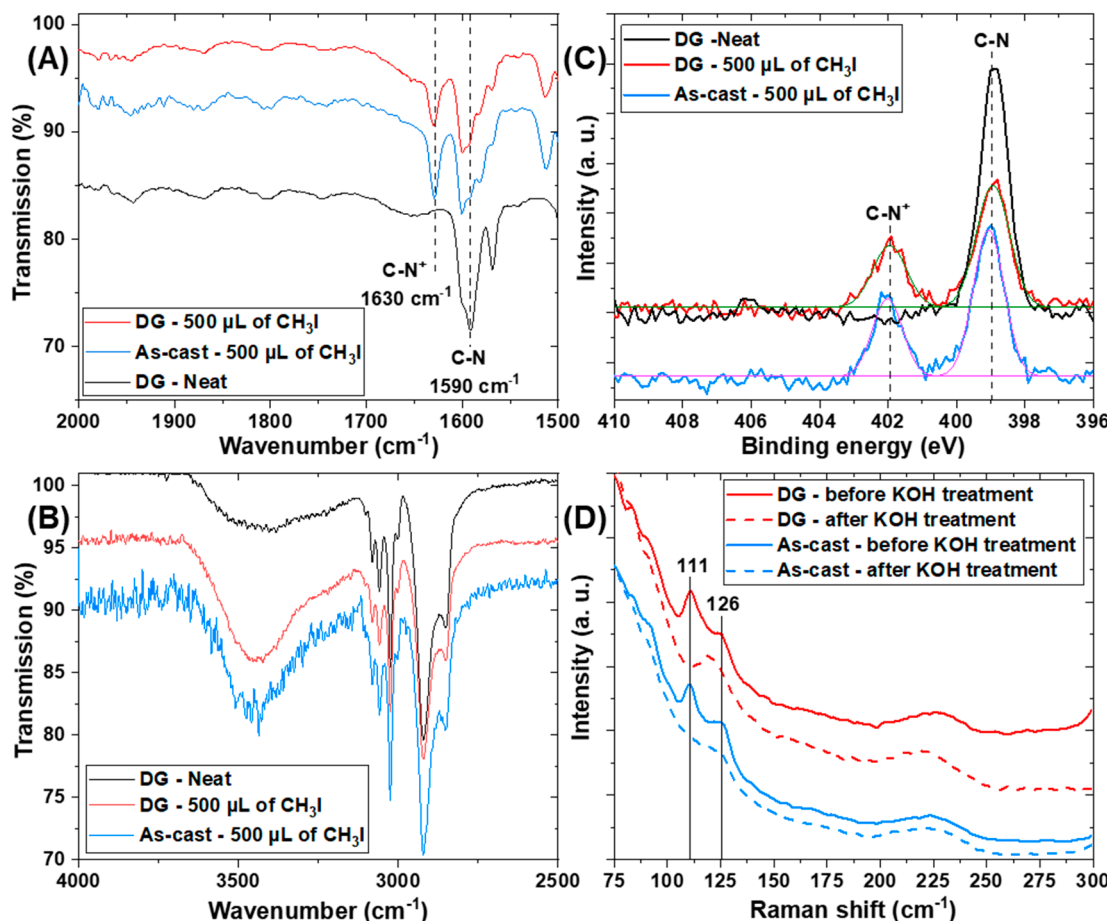


Figure 3. (A,B) FTIR spectra of neat and methylated DG-forming BCP films recorded in the regions of 1500–2000 cm^{-1} and 2000–4000 cm^{-1} , respectively. After a 4 h methylation reaction at 25 °C in a sealed jar containing a 500 μL CH_3I solution, the appearance of a new C-N⁺ band at 1630 cm^{-1} and an increase in the intensity of the broad O-H band directly and indirectly attest to the formation of NMP⁺ centers. The FTIR spectra of the methylated as-cast AEM exhibit a similar behavior to that of its DG-forming BCP counterpart. (C) The N1s XPS spectrum of the neat DG-forming BCP film displays a peak at 398.9 eV corresponding to pyridine sites. A second peak at 401.9 eV, observed in the N1s XPS spectra of as-cast and DG-structured AEMs, confirms the partial formation of NMP⁺ cations during the Menshutkin reaction. (D) Raman spectra of as-cast and DG-structured AEMs recorded before and after immersion in a 1 M KOH solution for 2 days at 20 °C. After treatment, the disappearance of bands at 111 and 126 cm^{-1} clearly indicates that the I₃⁻ species were fully ion-exchanged by OH⁻ counter anions.

As we wanted to determine the ionic conductivity of *N*-methylpyridinium-containing PS-*b*-P2VP-*b*-PEO films in their hydroxide counter anion form, the iodide ions were ion-exchanged by submerging the as-cast and DG-structured AEMs in a 1 M KOH solution for 2 days at 20 °C. The Raman spectra presented in Figure 3D revealed that the iodide form contained in the as-cast and DG-structured films is mainly driven by the presence of I₃⁻ ions before the KOH treatment since an intense band at 111 cm^{-1} , assigned to the symmetrical stretching mode of I₃⁻ species, is clearly observed [34–36]. Note that the band at 126 cm^{-1} is attributed to the asymmetrical stretching mode of I₃⁻ ions [34]. Conversely, the

disappearance of peaks attributed to the I_3^- ions on the Raman spectra recorded after the KOH treatment indicates that the iodide species inside the as-cast and DG-structured AEMs were fully ion-exchanged by the OH^- counter anions. To gain insight into the distribution of *N*-methylpyridinium centers within the as-cast and DG-structured AEMs, the distribution of their iodide counter-ions was analyzed using energy-dispersive X-ray spectroscopy (EDX). These analyses were performed on cross-sectional SEM images by integrating the signal from different regions of interest (ROIs) selected near the top and bottom surfaces as well as in the center of the terpolymer membranes (see Figures S4 and S5). The EDX analyses confirmed the presence of the iodine element in both the NMP^+ -containing as-cast and DG-structured AEMs. Based on the quantitative elemental composition analyses, both the quaternized as-cast and DG-structured AEMs revealed that iodine is homogeneously distributed throughout their entire film thicknesses with an average concentration of ~9 mass.% (~1 at.%) (see Tables S1 and S2). Interestingly, the elemental composition analyses further confirmed that the iodide ions were quantitatively exchanged by immersing the as-cast and DG-structured AEMs in a 1 M KOH solution for 2 days at 20 °C since the I accumulation in the different ROIs was invariably found to be very low (~0.5 mass.%, ~0.1 at.%, see Figures S6 and S7 and Tables S3 and S4).

EDX data confirming the uniform accumulation of iodine within BCP AEMs endowed with a DIS or DG phase in their I_3^- form and revealing the quantitative replacement of I_3^- anions by hydroxide ions, are summarized in Table 1.

Table 1. EDX data indicating the concentration of iodine (% at. and mass.%) within BCP AEMs featuring a DIS or DG phase before and after the ion-exchange protocol. Iodine accumulation was measured near the top and bottom surfaces as well as in the middle of the BCP AEMs.

Sample	I_3^- Concentration Close to the AEM Top Surface		I_3^- Concentration in the Middle of the AEM		I_3^- Concentration Close to AEM Bottom Surface	
	at.%	mass.%	at.%	mass.%	at.%	mass.%
DG in its I_3^- form	0.99	9.37	0.97	9.24	0.88	9.41
DG in its OH^- form	0.06	0.62	0.03	0.52	0.07	0.69
DIS in its I_3^- form	0.95	9.00	0.99	9.39	0.84	8.01
DIS in its OH^- form	0.05	0.55	0.06	0.61	0.08	0.82

To determine whether the creation of 3D-interconnected ion-conducting nanochannels throughout the entire film thickness is beneficial for improving the ion transport within the *N*-methylpyridinium-containing PS-*b*-P2VP-*b*-PEO AEMs, the ICs of hydrated as-cast and DG-structured membranes in their OH^- counter anion form were measured by using electrochemical impedance spectroscopy (EIS) in a through-plane configuration at 20 °C (see Figure 4A). For this purpose, the as-cast and DG-structured membranes, initially in their I_3^- form, were immersed in a 1 M KOH solution for 2 days to exchange iodide ions for hydroxide ions and were subsequently rinsed with deionized (DI) water to remove residual KOH prior to being sandwiched between two gold-plated blocking electrodes for EIS measurements. Note that hydroxide ion conductivities were measured under atmospheric conditions, which may result in IC values being influenced (i.e., lowered) by carbonate formation [37]. The Nyquist plots revealed that the hydrated as-cast AEM having a substructure with a DIS phase exhibited a lower IC compared to its hydrated DG-forming BCP counterpart. Indeed, the IC values of the as-cast and DG-structured AEMs in their OH^- form were determined to be 1.2 and 2.8 $mS \cdot cm^{-1}$ at 20 °C, respectively, using an equivalent circuit model comprising a Warburg (*W*) element, which represents the blocked-diffusion of ions, an electrode resistance ($R_{electrode}$), and a parallel arrangement of

a resistor (R_{AEM}) and a capacitance (C_{AEM}). For comparison, a significantly higher IC of $14.2 \text{ mS}\cdot\text{cm}^{-1}$ was measured at 20°C for the well-known Sustainion® X37-50 Grade RT (50 μm thick) under similar conditions. The high OH^- transport value observed for the Sustainion® AEM is strongly associated with its higher water uptake (WU) ($>80\%$) [38], whereas both the as-cast and DG-structured AEMs exhibit much lower water uptake values ($WU_{\text{as-cast}} = 5.3\%$ and $WU_{\text{DG}} = 6.3\%$). For instance, the low WU of DG-structured AEMs in their OH^- form ensures that the periodicity of the characteristic double-wave pattern formed on the (211) plane (p_{211}) increases by less than 10% upon the transition from DG nanochannels in their neutral pyridine form ($p_{211,\text{pyridine}} = 139 \text{ nm}$) to their charged form with NMP^+ centers with OH^- as counter-ions ($p_{211,\text{NMP}^+\text{OH}^-} = 159 \text{ nm}$) (see Figure S8). Note that the WU value of both the as-cast and DG-structured AEMs weakly depends on the degree of pyridine conversion into NMP^+ centers since disordered and ordered neutral PS-*b*-P2VP-*b*-PEO membranes exhibit similar WU values. This behavior is probably due to the good hydrophilicity of the nanopathway-forming PEO block. While it is admitted that a low WU is preferred to preserve the mechanical integrity of BCP membranes after drying, the presence of nanochannels within the AEM plays a prominent role in achieving superior mechanical properties. Indeed, only the DG-forming BCP AEMs in their I_3^- form maintain a measurable Young's modulus ($>10 \text{ MPa}$ over a 0°C to 100°C range, see Figure S9) in the dried state whereas dried as-cast counterparts systematically experience mechanical failures that compromise their structural integrity. Note also that the featureless Sustainion® X37-50 Grade RT membrane is known for its brittleness and susceptibility to cracking when dry, owing to its polystyrene composition [39].

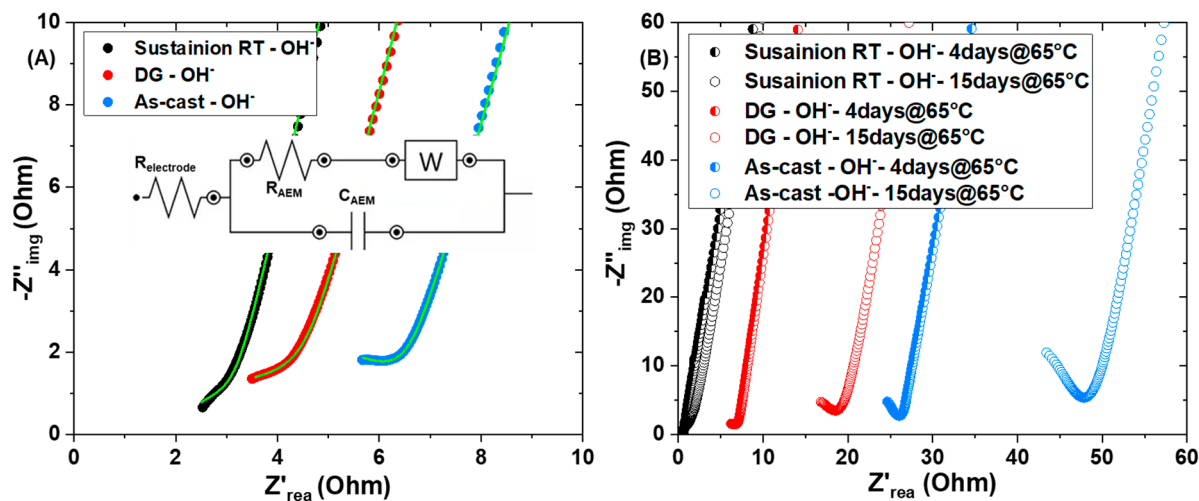


Figure 4. (A) Nyquist plots obtained at 20°C from hydrated (blue) as-cast and (red) DG-structured AEMs that were immersed in a 1 M KOH solution for 2 days before being rinsed with DI water to remove excess KOH. The different ICs were fitted using the equivalent circuit model in the inset to extract the R_{AEM} values (see green fitting curves). (B) Nyquist plots measured at 20°C from hydrated (blue) as-cast and (red) DG-structured AEMs that were immersed in a 1 M KOH solution maintained at 65°C for 4 or 15 days before being rinsed with DI water to remove excess KOH. In (A,B), data obtained for a similarly conditioned (black) Sustainion® AEM are shown for comparison.

The chemical stability of as-cast and DG-structured AEMs in alkaline media was also evaluated by immersing the membranes in a 1 M KOH solution heated at 65°C for up to 15 days, followed by a DI water rinsing to reach a neutral pH (Figure 4B). Over the ageing period, the IC of the as-cast AEM decreased more rapidly than that of the DG-forming membrane. For example, after 4 days, IC values of 0.3 and $2.6 \text{ mS}\cdot\text{cm}^{-1}$ were measured for the as-cast and DG-structured AEMs, respectively. These $\sigma_{\text{as-cast}}$ and σ_{DG} values

stabilized at 0.2 and 0.5 $\text{mS}\cdot\text{cm}^{-1}$ after 15 days. By contrast, the IC values of the tetramethyl imidazolium-containing Sustainion® AEM were determined to be 14.2 and 13.6 $\text{mS}\cdot\text{cm}^{-1}$ after 4 and 15 days of ageing under the same conditions. While the imidazolium functional group demonstrated greater stability than the cationic NMP^+ center in a heated alkaline environment, EIS measurements fully support the benefits of incorporating ion-conducting DG nanochannels throughout the film thickness to enhance ion transport in NMP^+ -based BCP AEMs. Note that the degradation of the NMP^+ cation in its OH^- form is due to its poor stability in an alkaline environment, especially at elevated temperatures, where the hydroxyl ion attacks the cation at the ortho position, degrading it into 2-pyridone through irreversible oxidation, resulting in charge loss [40].

Apart from the need for manufacturing fast ion-conducting nanochannels to minimize Ohmic losses, it is admitted that AEMs would have high water permeability in order to offset the critical issues of water management via a rapid back diffusion of liquid water from the anode to the cathode. To know more about the water transport properties of the hydrophilic DG nanochannels in which pyridine sites were partly converted (~52%) to NMP^+ cations with iodides as counter-ions, liquid–liquid water permeation (LLP) measurements were performed (see Figure 5). For that purpose, the change in water flux, J , of a quaternized DG-forming PS-*b*-P2VP-*b*-PEO film deposited on porous ($0.1 \mu\text{m}$) hydrophilic PVDF support has been plotted as a function of the water pressure applied from 0.5 to 2.0 bar, using a dead-end stirred ultrafiltration cell. From the slope of the linear fit, a mean water permeance value of $\sim 384 \text{ L h}^{-1} \text{ m}^{-2} \text{ bar}^{-1}$ was determined based on three different samples, and the value of the coefficient of determination, R^2 , close to unity ($R^2 \approx 0.99$) indicates that the DG-forming AEM in its iodide form possesses excellent stability to material failure even at 2 bar (water conditions: $\text{pH} = 7$ and $T = 20^\circ\text{C}$). Note that the thickness-normalized permeability value established for this AEM in its iodide form ($\sim 2.6 \times 10^{-14} \text{ m}^2 \text{ Pa}^{-1} \text{ s}^{-1}$) is twice as high as that previously measured for neutral DG-structured counterparts ($\sim 1.1 \times 10^{-14} \text{ m}^2 \text{ Pa}^{-1} \text{ s}^{-1}$)²⁹ but is very close to the normalized permeability of a $50 \mu\text{m}$ -thick Sustainion® AEM ($\sim 2.5 \times 10^{-14} \text{ m}^2 \text{ Pa}^{-1} \text{ s}^{-1}$) since its water permeance value was determined to be of $\sim 200 \text{ L h}^{-1} \text{ m}^{-2} \text{ bar}^{-1}$. Finally, no flux was measured from the as-cast PS-*b*-P2VP-*b*-PEO film even under a pressure drop (ΔP) of 2 bar indicating that no water molecule can pass through its dense substructure due to the lack of nanochannel formation.

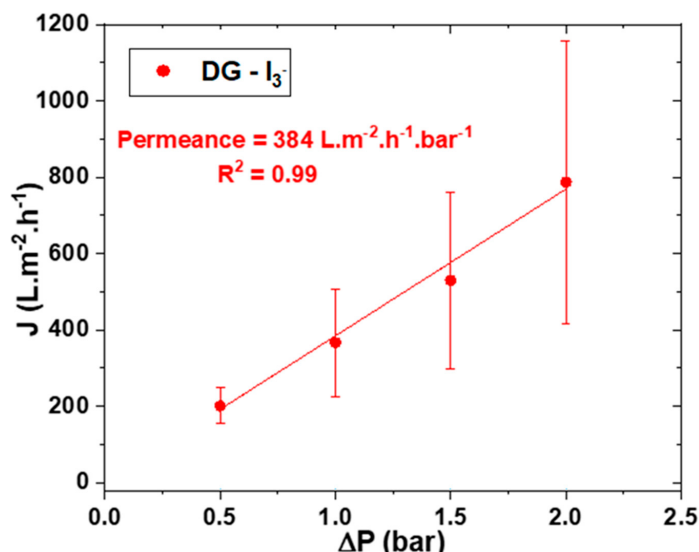


Figure 5. Water flux, J , of a PS-*b*-P2VP-*b*-PEO AEM endowed with NMP^+ -containing DG nanochannels. Error bars are the standard deviations of the mean relative permeability values calculated for three different samples.

3. Conclusions

In this work, *N*-methylpyridinium-containing BCP AEMs endowed with highly permeable ion-conducting DG nanochannels were manufactured by using a SVA-methylation strategy. This 3D-interconnected morphology, with intrinsically good mechanical properties and moderate tortuosity, allows the water and ion transport of PS-*b*-P2VP-*b*-PEO AEMs to be enhanced compared to the nominal disordered phase (i.e., the as-cast morphology). For instance, our results show that creating NMP⁺-based DG nanochannels within hydrated BCP AEMs in their OH⁻ counter ion form enables to achieve IC and permeance values as high as 2.8 mS.cm⁻¹ and 384 L h⁻¹ m⁻² bar⁻¹ at 20 °C, respectively. Conversely, a lower IC value of ~1.2 S.cm⁻¹ was measured at 20 °C from an analog hydrated BCP AEM having a non-permeable DIS phase. Such DG-forming BCP AEMs offering low Ohmic resistance and high permeability could be useful to permeate the large amount of water generated at the anode, thus mitigating the anode flooding and cathode drying that invariably occur in AEMFCs.

4. Experimental

Material: 1,4-Dioxane (DOX, 99.5%), tetrahydrofuran (THF, 99%), dichloromethane (DCM, 99%), methyl iodide (CH₃I, >99%), and poly(3,4-ethylenedioxythiophene):polystyrene sulfonate (PEDOT:PSS, 2.8% wt. in water) were purchased from Sigma Aldrich (Saint-Quentin-Fallavier, France). Silicon substrates were provided from Silicon Materials (Si-Mat, Kaufering, Germany). PS-*b*-P2VP-*b*-PEO (S:2VP:EO ≈ 65:22:13, 69.5 kg.mol⁻¹) was purchased from Polymer Source Inc. (Dorval, QC, Canada). The 50 μm-thick Sustainion® X37-50 Grade RT membranes were provided from Dioxide Materials (Boca Raton, FL, USA).

Fabrication of as-cast and DG-structured PS-*b*-P2VP-*b*-PEO layers: The 25 μm-thick PS-*b*-P2VP-*b*-PEO films having a substructure with a disordered phase were cast from a 20% wt terpolymer solution in a di-solvent mixture (DOX/THF: 70/30 by weight) onto (3 × 3 cm) silicon substrates, covered by a sacrificial PEDOT:PSS layer, by using a tape casting technique with a 400 μm blade gap. To produce nanostructured PS-*b*-P2VP-*b*-PEO films, the as-cast layers were exposed to a DCM vapor for 15 h in order to promote the mobility of terpolymer chains until reaching the formation of the DG morphology. Here, a continuous flow system was used to control the DCM vapor pressure (32 sccm DCM + 8 sccm N₂) in the SVA chamber as described previously [41]. Note that the temperature of the DCM tank was kept at 20 °C during the SVA process. Regarding this process protocol, a DCM vapor was used instead of chloroform (CHCl₃) because it ensures the formation of a DG morphology from neat PS-*b*-P2VP-*b*-PEO films, whereas a blend with PS-*b*-PEO chains was necessary to produce this TPMS structure under a CHCl₃ vapor [29]. In addition, as the SVA duration required to achieve a PS-*b*-P2VP-*b*-PEO film entirely composed of a well-developed DG structure is highly dependent on both the relative humidity (RH) and temperature of the laboratory (the SVA duration must be increased with the RH value), BCP AEMs were overexposed to a DCM vapor. Notably, a 4 h SVA duration is sufficient to achieve a complete DG structure during a summer day with a low RH.

Fabrication of as-cast and DG-structured PS-*b*-P2VP-*b*-PEO AEMs in their I₃⁻ and OH⁻ forms: To produce *N*-methylpyridinium-containing PS-*b*-P2VP-*b*-PEO membranes, the as-cast and DG-structured films were exposed to a CH₃I vapor for 4 h in a sealed jar maintained at 25 °C. Freestanding PS-*b*-P2VP-*b*-PEO AEMs in their I₃⁻ form were obtained by solubilizing the sacrificial PEDOT:PSS layer in a deionized water bath. To prepare the BCP AEMs in their OH⁻ form, the iodide ions were ion-exchanged by submerging the as-cast and DG-structured terpolymer layer in a 1 M KOH solution for 2 days at 20 °C. This ion-exchange protocol was used to ensure that as-cast PS-*b*-P2VP-*b*-PEO AEMs were produced in their complete OH⁻ form, noting that BCP films featuring a DIS phase are non-

permeable, while, fortunately, pyridinium degradation by OH⁻ attack is less effective at 20 °C. The chemical stability of BCP AEMs in alkaline media was evaluated by immersing the membranes in a 1 M KOH solution heated to 65 °C for up to 15 days. Note that all BCP AEMs were washed in a deionized water bath prior to each ionic conductivity measurement.

Ionic conductivity, DMA, and water flux measurements: The ionic conductivities of 25 µm-thick AEMs with a DIS or DG phase were recorded by using electrochemical impedance spectroscopy (Solartron 1260 impedance analyzer, AMETEK SAS, Elancourt, France) over a frequency range between 1 MHz and 1000 Hz with an amplitude of 50 mV. For that purpose, the hydrated as-cast and DG-structured AEMs in their OH⁻ form were placed into a sample holder (BioLogic CESH-e, Biologic, Seyssinet-Pariset, France) with circular gold-plated blocking electrodes (1/2" diameter), and then compressed to allow through-plane measurements at 20 °C. Thermomechanical properties (elastic storage modulus, E') of a 25 µm-thick DG-structured AEM in its I₃⁻ form were assessed using a DMA 242 E Artemis from NETZSCH (Lyon, France). The sample was heated from 0 °C to over 100 °C at a rate of 2 °C·min⁻¹, with a frequency of 1 Hz and a displacement amplitude of 10 µm (0.1% strain). The water permeability of freestanding DG-structured PS-*b*-P2VP-*b*-PEO AEMs in their I₃⁻ form were measured in a 10 mL filtration cell (Amicon 8010 stirred cell) connected to a water reservoir and a compressed air line. The measurements were performed on 2.5 cm diameter PS-*b*-P2VP-*b*-PEO material discs supported by a high permeable hydrophilic PVDF material [29] at pressures between 0.5 and 2 bar. The mass of water passing through the stacked materials (permeate) was recorded using a connected balance at regular time intervals for 7 min. Water temperature was maintained at 20 °C during the measurements while the error bars were calculated from 3 different samples. In order to avoid a non-linear behavior of the water flux with the increase in pressure drop, a transmembrane pressure of 2.5 bar was applied during 10 min prior to the measurements to determine their permeability performance.

AFM and SEM imaging and EDX analyses: Atomic force microscopy (AFM Nano-Observer, CSInstruments, Les Ulis, France) was used in tapping mode to characterize the surface morphology of PS-*b*-P2VP-*b*-PEO films. Silicon cantilevers (PPP-NCH, Nanosensors, NanoAndMore, Paris, France) with a typical tip radius of ~5 nm were used. The resonance frequency of cantilevers was ~235 kHz. Scanning electron microscopy (SEM, Hitachi S-4800, Tokyo, Japan) was used at an accelerating voltage of 5 kV to acquire top view and cross-section images of both as-cast and DG-structured films. EDX analyses were conducted inside a Zeiss Sigma 300 SEM (Oberkochen, Germany) using an Oxford Instruments X-Max^N 50 mm² Silicon Drift Detector (High Wycombe, UK).

FTIR, XPS, and Raman measurements: FTIR spectra were monitored on a Thermo Nicolet Nexus FTIR spectrometer (ThermoFisher Scientific, Illkirch-Graffenstaden, France) with a diamond ATR attachment, and samples were subjected to 32 scans in the range of 4000 and 650 cm⁻¹. XPS was performed on an ESCALAB 250 (Thermo Electron Scientific, Illkirch-Graffenstaden, France) with a monochromatic Al K α (1486.6 eV) source operating at 150 W (15 kV and 10 mA). The analyzed surface area was 500 µm² with a sampling depth of ~5 nm. The emitted photoelectrons were detected perpendicular to the sample surface with a constant analyzer energy mode. Data analysis was carried out using the Avantage software V5. Binding energies (BEs) of all core levels are referred to the C-C bond of C1s (at 284.8 eV). The charge is compensated by a low energy (~2 eV) electron beam. N1s and I3d high-resolution spectra were recorded at a step of 0.1 eV (transition energy of 20 eV). Micro-Raman analyses were conducted using a HORIBA Jobin LabRAM HR800UV Raman spectrometer (λ = 660 nm, 1800 gr·mm⁻¹ grating) with a Leica PL Fluotar \times 50 objective (NA = 0.55). Si vibration at 520 cm⁻¹ was employed for calibration. Raman spectra were

typically collected with 60 s exposure time and 4 accumulations at a laser power of 10 mW. No post-processing was performed on obtained data.

Supplementary Materials: The following supporting information can be downloaded at: <https://www.mdpi.com/article/10.3390/batteries11040126/s1>, Figure S1: Cross-sectional SEM views of an as-cast PS-*b*-P2VP-*b*-PEO film; Figure S2: AFM topographic image showing the bottom's surface of a DG structured DG-structured PS-*b*-P2VP-*b*-PEO film; Figure S3: I3d XPS spectra of as-cast and DG-structured PS-*b*-P2VP-*b*-PEO films; Figure S4: Cross-sectional SEM image of a DG-forming BCP AEM in its iodide form showing four EDX ROIs; Table S1: Analysis table results of the four EDX-ROIs for the DG-forming BCP AEM in its iodide form; Figure S5: Cross-sectional SEM image of an as-cast BCP AEM in its iodide form showing four EDX ROIs; Table S2: Analysis table results of the four EDX-ROIs for the as-cast BCP AEM in its iodide form; Figure S6: Cross-sectional SEM image of a DG-forming BCP AEM in its hydroxide form showing four EDX ROIs; Table S3: Analysis table results of the four EDX-ROIs for the DG-forming BCP AEM in its hydroxide form; Figure S7: Cross-sectional SEM image of an as-cast BCP AEM in its hydroxide form showing four EDX ROIs; Table S4: Analysis table results of the four EDX-ROIs for the as-cast BCP AEM in its hydroxide form; Figure S8: AFM topographic images of a DG-structured PS-*b*-P2VP-*b*-PEO film taken after the formation of NMP^+OH^- charges within the DG nanochannels; Figure S9: Storage modulus versus temperature of a DG-forming BCP AEM in its iodide form.

Author Contributions: Conceptualization, K.A.; methodology, K.A.; software, E.P. (Erwan Ponsin), J.R. and C.B.-H.; validation, K.A., D.Q. and S.R.; formal analysis, M.C.; investigation, K.A., S.V. and E.P. (Eddy Petit); resources, K.A.; data curation, B.R., C.B.-H. and J.R.; writing—original draft preparation, K.A.; writing—review and editing, K.A., D.Q. and S.R.; visualization, K.A.; supervision, K.A.; project administration, K.A.; funding acquisition, K.A. All authors have read and agreed to the published version of the manuscript.

Funding: This research received no external funding.

Data Availability Statement: The data presented in this study are available on request from the corresponding author.

Acknowledgments: The authors thank the Balard Analysis and Characterizations Platform (UAR 2041 PAC Chimie Balard Montpellier) facilities for technical support.

Conflicts of Interest: The authors declare no conflict of interest.

References

1. Yang, Y.; Peltier, C.R.; Zeng, R.; Schimmenti, R.; Li, Q.; Huang, X.; Yan, Z.; Potsi, G.; Selhorst, R.; Lu, X.; et al. Electrocatalysis in Alkaline Media and Alkaline Membrane-Based Energy Technologies. *Chem. Rev.* **2022**, *122*, 6117–6321.
2. Das, G.; Choi, J.H.; Nguyen, P.K.; Kim, D.J.; Yoon, Y.S. Anion Exchange Membranes for Fuel Cell Application: A Review. *Polymers* **2022**, *14*, 1197. [[CrossRef](#)] [[PubMed](#)]
3. Park, E.J.; Jannasch, P.; Miyatake, K.; Bae, C.; Noonan, K.; Fujimoto, C.; Holdcroft, S.; Varcoe, J.R.; Henkensmeier, D.; Guiver, M.D.; et al. Aryl ether-free polymer electrolytes for electrochemical and energy devices. *Chem. Soc. Rev.* **2024**, *53*, 5704. [[CrossRef](#)] [[PubMed](#)]
4. Song, W.; Zhang, X.; Yang, C.; Yang, Z.; Wu, L.; Ge, X.; Xu, T. Alkaline Membranes Toward Electrochemical Energy Devices: Recent Development and Future Perspectives. *ACS Cent. Sci.* **2023**, *9*, 1538. [[PubMed](#)]
5. Hu, C.; Wang, Y.; Lee, Y.M. Ether-Free Alkaline Polyelectrolytes for Water Electrolyzers: Recent Advances and Perspectives. *Angew. Chem. Int. Ed.* **2024**, *64*, e202418324.
6. Peron, J.; Mani, A.; Zhao, X.S.; Edwards, D.; Adachi, M.; Soboleva, T.; Shi, Z.Q.; Xie, Z.; Navessin, T.; Holdcroft, S. Properties of Nafion (R) Nr-211 Membranes for Pemfc's. *J. Membr. Sci.* **2010**, *356*, 44–51.
7. Omasta, T.J.; Peng, X.; Miller, H.A.; Vizza, F.; Wang, L.; Varcoe, J.R.; Dekel, D.; Mustain, W.E. Beyond 1.0W cm^{-2} Performance without Platinum: The Beginning of a New Era in Anion Exchange Membrane Fuel Cells. *J. Electrochem. Soc.* **2018**, *165*, J3039–J3044.
8. Dekel, D.R. Review of Cell Performance in Anion Exchange Membrane Fuel Cells. *J. Power Sources* **2018**, *375*, 158–169.

9. Buggy, N.C.; Du, Y.; Kuo, M.-C.; Ahrens, K.A.; Wilkinson, J.S.; Seifert, S.; Coughlin, E.B.; Herring, A.M. A Polyethylene-Based Triblock Copolymer Anion Exchange Membrane with High Conductivity and Practical Mechanical Properties. *ACS Appl. Polym. Mater.* **2020**, *2*, 1294–1303.
10. Luo, X.; Wright, A.; Weissbach, T.; Holdcroft, S. Water Permeation through Anion Exchange Membranes. *J. Power Sources* **2018**, *375*, 442–451.
11. Dekel, D.R.; Amar, M.; Willdorf, S.; Kosa, M.; Dhara, S.; Diesendruck, C.E. Effect of Water on the Stability of Quaternary Ammonium Groups for Anion Exchange Membrane Fuel Cell Applications. *Chem. Mater.* **2017**, *29*, 4425–4431.
12. Li, N.; Guiver, M.D. Ion Transport by Nanochannels in Ion-Containing Aromatic Copolymers. *Macromolecules* **2014**, *47*, 2175–2198.
13. Shin, D.W.; Guiver, M.D.; Lee, Y.M. Hydrocarbon-Based Polymer Electrolyte Membranes: Importance of Morphology on Ion Transport and Membrane Stability. *Chem. Rev.* **2017**, *117*, 4759–4805.
14. Price, S.C.; Ren, X.; Jackson, A.C.; Ye, Y.; Elabd, Y.A.; Beyer, F.L. Bicontinuous Alkaline Fuel Cell Membranes from Strongly Self-Segregating Block Copolymers. *Macromolecules* **2013**, *46*, 7332–7340.
15. Ye, Y.; Choi, J.H.; Winey, K.I.; Elabd, Y.A. Polymerized Ionic Liquid Block and Random Copolymers: Effect of Weak Microphase Separation on Ion Transport. *Macromolecules* **2012**, *45*, 7027–7035.
16. Li, Y.; Liu, Y.; Savage, A.M.; Beyer, F.L.; Seifert, S.; Herring, A.M.; Knauss, D.M. Polyethylene-Based Block Copolymers for Anion Exchange Membranes. *Macromolecules* **2015**, *48*, 6523–6533.
17. Tsai, T.H.; Maes, A.M.; Vandiver, M.A.; Versek, C.; Seifert, S.; Tuominen, M.; Liberatore, M.W.; Herring, A.M.; Coughlin, E.B. Synthesis and Structure-Conductivity Relationship of Polystyrene-Block- Poly(Vinyl Benzyl Trimethylammonium) for Alkaline Anion Exchange Membrane Fuel Cells. *J. Polym. Sci. Part B Polym. Phys.* **2013**, *51*, 1751–1760.
18. Sun, L.; Guo, J.; Zhou, J.; Xu, Q.; Chu, D.; Chen, R. Novel Nanostructured High-Performance Anion Exchange Ionomers for Anion Exchange Membrane Fuel Cells. *J. Power Sources* **2012**, *202*, 70–77.
19. Ye, Y.; Sharick, S.; Davis, E.M.; Winey, K.I.; Elabd, Y.A. High Hydroxide Conductivity in Polymerized Ionic Liquid Block Copolymers. *ACS Macro Lett.* **2013**, *2*, 575–580.
20. Chen, Z. Water Balancing. *Nat. Energy* **2020**, *5*, 12–13.
21. Mandal, M.; Huang, G.; Hassan, N.U.; Peng, X.; Gu, T.; Brooks-Starks, A.H.; Bahar, B.; Mustain, W.E.; Kohl, P.A. The Importance of Water Transport in High Conductivity and High-Power Alkaline Fuel Cells. *J. Electrochem. Soc.* **2020**, *167*, 054501. [\[CrossRef\]](#)
22. Mustain, W.E. Understanding How High-Performance Anion Exchange Membrane Fuel Cells Were Achieved: Component, Interfacial, and Cell-Level Factors. *Curr. Opin. Electrochem.* **2018**, *12*, 233–239. [\[CrossRef\]](#)
23. Dekel, D.R.; Willdorf, S.; Ash, U.; Amar, M.; Pusara, S.; Dhara, S.; Srebnik, S.; Diesendruck, C.E. The Critical Relation between Chemical Stability of Cations and Water in Anion Exchange Membrane Fuel Cells Environment. *J. Power Sources* **2018**, *375*, 351–360. [\[CrossRef\]](#)
24. Aissou, K.; Mumtaz, M.; Hermida-Merino, D.; Solano, E.; Cot, D.; Tarek Benkhaled, B.; Quémener, D.; Roualdes, S.; Fleury, G.; Hadzioannou, G. Square arrays of vertically aligned nanoporous cylinders from a linear ABC triblock terpolymer. *J. Polym. Sci.* **2023**, *61*, 1259. [\[CrossRef\]](#)
25. Arges, C.G.; Kambe, Y.; Suh, H.S.; Ocola, L.E.; Nealey, P.F. Perpendicularly aligned, anion conducting nanochannels in block copolymer electrolyte films. *Chem. Mater.* **2016**, *28*, 1377–1389. [\[CrossRef\]](#)
26. Kambe, Y.; Arges, C.G.; Czaplewski, D.A.; Dolejsi, M.; Krishnan, S.; Stoykovich, M.P.; de Pablo, J.J.; Nealey, P.F. Role of Defects in Ion Transport in Block Copolymer Electrolytes. *Nano Lett.* **2019**, *19*, 4684–4691. [\[CrossRef\]](#)
27. Luo, J.-W.; Chen, L.; Min, T.; Shan, F.; Kang, Q.; Tao, W. Macroscopic transport properties of Gyroid structures based on pore-scale studies: Permeability, diffusivity and thermal conductivity. *Int. J. Heat Mass Tran.* **2020**, *146*, 118837. [\[CrossRef\]](#)
28. Yan, L.; Rank, C.; Mecking, S.; Winey, K.I. Gyroid and Other Ordered Morphologies in Single-Ion Conducting Polymers and Their Impact on Ion Conductivity. *J. Am. Chem. Soc.* **2020**, *142*, 857. [\[CrossRef\]](#) [\[PubMed\]](#)
29. Aissou, K.; Coronas, M.; Hermida-Merino, D.; Solano, E.; Cot, D.; Roualdes, S.; Bouyer, D.; Quemener, D. Nanoporous Double-Gyroid Structure from ABC Triblock Terpolymer Thick Films. *Int. J. Polym. Sci.* **2023**, *2023*, 9598572. [\[CrossRef\]](#)
30. Johnson, C.W.; Zhang, L.; Culley, K.E.; Oh, S.M.; Gin, D.L.; Geise, G.M.; Patel, A.J.; Winey, K.I.; Osuji, C.O. The Effects of Morphology and Hydration on Anion Transport in Self-Assembled Nanoporous Membranes. *ACS Nano* **2025**, *19*, 2559. [\[CrossRef\]](#)
31. Choi, J.H.; Ye, Y.S.; Elabd, Y.A.; Winey, K.I. Network Structure and Strong Microphase Separation for High Ion Conductivity in Polymerized Ionic Liquid Block Copolymers. *Macromolecules* **2013**, *46*, 5290.
32. Kumar, R.; Muthukumar, M. Microphase separation in polyelectrolytic diblock copolymer melt: Weak segregation limit. *J. Chem. Phys.* **2007**, *126*, 214902. [\[PubMed\]](#)
33. Marko, J.F.; Rabin, Y. Microphase Separation of Charged Diblock Copolymers: Melts and Solutions. *Macromolecules* **1992**, *25*, 1503.
34. Ordinartsev, A.A.; Petrov, A.A.; Lyssenko, K.A.; Petrov, A.V.; Goodilin, E.A.; Tarasov, A.B. Crystal structure of new formamidinium triiodide jointly refined by single-crystal XRD, Raman scattering spectroscopy and DFT assessment of hydrogen-bond network features. *Acta Crystallogr. Sect. E Crystallogr. Commun.* **2021**, *77*, 692–695.

35. Deplano, P.; Ferraro, J.R.; Mercuri, M.L.; Trogu, E.F. Structural and Raman spectroscopic studies as complementary tools in elucidating the nature of the bonding in polyiodides and in donor-I₂ adducts. *Coord. Chem. Rev.* **1999**, *188*, 71–95.
36. Spadoni, A.; Falconieri, M.; Lanchi, M.; Liberatore, R.; Marrocco, M.; Sau, G.S.; Tarquini, P. Iodine compounds speciation in HI-I₂ aqueous solutions by Raman spectroscopy. *Int. J. Hydrogen Energy* **2012**, *37*, 1326–1334.
37. Siroma, Z.; Watanabe, S.; Yasuda, K.; Fukuta, K.; Yanagi, H. Mathematical Modeling of the Concentration Profile of Carbonate Ions in an Anion Exchange Membrane Fuel Cell. *ECS Trans.* **2010**, *33*, 1935. [[CrossRef](#)]
38. Rodriguez, C.A.G.; Joensen, B.Ó.; Moss, A.B.; Larrazábal, G.O.; Whelligan, D.K.; Seger, B.; Varcoe, J.R.; Willson, T.R. Influence of Headgroups in Ethylene-Tetrafluoroethylene-Based Radiation-Grafted Anion Exchange Membranes for CO₂ Electrolysis. *ACS Sustain. Chem. Eng.* **2023**, *11*, 1508. [[CrossRef](#)]
39. Wijaya, G.H.A.; Im, K.S.; Nam, S.Y. Advancements in commercial anion exchange membranes: A review of membrane properties in water electrolysis applications. *Desalin. Water Treat.* **2024**, *320*, 100605.
40. Voge, A.; Deimede, V.; Kallitsis, J.K. Synthesis and properties of alkaline stable pyridinium containing anion exchange membranes. *RSC Adv.* **2014**, *4*, 45040.
41. Aissou, K.; Bouzit, H.; Krusch, F.; Méricq, J.-P.; Cot, D.; Masquelez, N.; Roualdes, S.; Quémener, D. Asymmetric Solvent-Annealed Triblock Terpolymer Thick Films Topped by a Hexagonal Perforated Lamellar Nanostructure. *Macromol. Rapid Commun.* **2022**, *43*, 2100585.

Disclaimer/Publisher's Note: The statements, opinions and data contained in all publications are solely those of the individual author(s) and contributor(s) and not of MDPI and/or the editor(s). MDPI and/or the editor(s) disclaim responsibility for any injury to people or property resulting from any ideas, methods, instructions or products referred to in the content.